Local structure and ionic conductivity in the $Zr_2Y_2O_7$–Y_3NbO_7 system

2009 J. Phys.: Condens. Matter 21 215401

(http://iopscience.iop.org/0953-8984/21/21/215401)

J. Phys.: Condens. Matter **21** (2009) 215401 (11pp) doi:10.1088/0953-8984/21/21/215401

Local structure and ionic conductivity in the $Zr_2Y_2O_7$–Y_3NbO_7 system

Stefan T Norberg[1,2,5], Istaq Ahmed[1,2], Stephen Hull[1], Dario Marrocchelli[3] and Paul A Madden[3,4]

[1] The ISIS Facility, Rutherford Appleton Laboratory, Chilton, Didcot, Oxfordshire OX11 0QX, UK
[2] Department of Chemical and Biological Engineering, Chalmers University of Technology, SE-412 96 Gothenburg, Sweden
[3] School of Chemistry, Edinburgh University, The King's Building, West Mains Road, Edinburgh EH9 3JJ, UK
[4] Department of Materials, University of Oxford, Oxford OX1 3PH, UK

E-mail: stn@chalmers.se

Received 28 January 2009, in final form 20 March 2009
Published 29 April 2009
Online at stacks.iop.org/JPhysCM/21/215401

Abstract

The $Zr_{0.5-0.5x}Y_{0.5+0.25x}Nb_{0.25x}O_{1.75}$ solid solution possesses an anion-deficient fluorite structure across the entire $0 \leqslant x \leqslant 1$ range. The relationship between the disorder within the crystalline lattice and the preferred anion diffusion mechanism has been studied as a function of x, using impedance spectroscopy measurements of the ionic conductivity (σ), powder neutron diffraction studies, including analysis of the 'total' scattering to probe the nature of the short-range correlations between ions using reverse Monte Carlo (RMC) modelling, and molecular dynamics (MD) simulations using potentials derived with a strong *ab initio* basis. The highest total ionic conductivity ($\sigma = 2.66 \times 10^{-2}\ \Omega^{-1}\ cm^{-1}$ at 1473 K) is measured for the $Zr_2Y_2O_7$ ($x = 0$) end member, with a decrease in σ with increasing x, whilst the neutron diffraction studies show an increase in lattice disorder with x. This apparent contradiction can be understood by considering the local structural distortions around the various cation species, as determined from the RMC modelling and MD simulations. The addition of Nb^{5+} and its stronger Coulomb interaction generates a more disordered local structure and enhances the mobility of some anions. However, the influence of these pentavalent cations is outweighed by the effect of the additional Y^{3+} cations introduced as x increases, which effectively trap many anions and reduce the overall concentration of the mobile O^{2-} species.

1. Introduction

Materials with high values of oxide-ion conductivity are currently the subject of extensive research activity, motivated by their technological applications within solid oxide fuel cells (SOFCs), oxygen separation membranes and gas sensors. Binary compounds of stoichiometry AO_2 possessing the cubic fluorite structure (figure 1) are of particular interest, especially when some of the host cations are replaced by species of a lower valence to produce anion-deficient phases (e.g. $A^{4+}_{1-x}B^{3+}_xO_{2-x/2}$ or $A^{4+}_{1-x}B^{2+}_xO_{2-x}$). The charge compensating vacancies formed on the anion sublattice become mobile at elevated temperatures, leading to the impressive ionic conductivities shown by, for example, zirconia (ZrO_2) ceramics doped with trivalent cations such as Y^{3+}, Sc^{3+} and the rare earths [1].

The highest ionic conductivities for zirconias are found in those doped with Sc^{3+}, though such samples have a number of drawbacks in terms of cost and long-term stability [2]. As a consequence, the most widely used compounds are formed by doping with Y^{3+}. In the $Zr_{1-x}Y_xO_{2-x/2}$ system, the monoclinic baddelyite structure adopted by pure ZrO_2 transforms to a tetragonally distorted fluorite phase (t^*) at $x \approx 0.05$ and to the cubic fluorite phase (c^*) at $x \approx 0.16$ [3]. The ionic conductivity increases initially with x due to the increasing concentration of O^{2-} vacancies, but reaches a maximum ($\sigma \sim 10^{-2}\ \Omega^{-1}\ cm^{-1}$ at 1000 K [4])

[5] Author to whom any correspondence should be addressed.

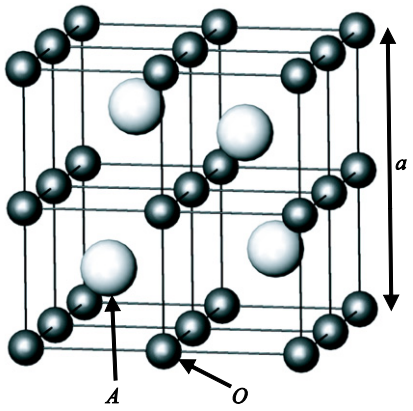

Figure 1. The cubic fluorite structure of a compound of stoichiometry AO_2 in space group $Fm\bar{3}m$, with cations at the 4(a) sites at 0, 0, 0, etc and the oxygen atoms at the 8(c) sites at 1/4, 1/4, 1/4 etc.

at close to the lower stability limit of the c* phase and then falls rapidly. The latter behaviour has been attributed to the increased lattice strain induced by the size mismatch between host and dopant cations and to the formation of defect clusters which effectively trap the mobile vacancies [5–9]. The nature of the structural defects within $Zr_{1-x}Y_xO_{2-x/2}$ at relatively high values of x has been the subject of considerable debate within the literature (for references, see [10]), with evidence favouring the formation of clusters which resemble the (long-range ordered) structure of the phase $Zr_3Y_4O_{12}$ [11, 12].

Compounds of stoichiometry M_3NbO_7 and M_3TaO_7 are also known to adopt anion-deficient fluorite structures, provided the trivalent M cations are relatively small [13–16]. In the case of Y_3NbO_7, the diffuse scattering observed within x-ray diffraction patterns has been interpreted in terms of small domains possessing a pyrochlore-type structure [17], though diffuse spots seen in electron diffraction images favoured a more complex two-dimensional anti-phase structure [18]. However, the ionic conductivity of Y_3NbO_7 ($\sigma \sim 2 \times 10^{-5}$ Ω^{-1} cm^{-1} at 1000 K [17]) is significantly lower than that of $Zr_{1-x}Y_xO_{2-x/2}$. Whilst this precludes any applications of Y_3NbO_7 as an oxide-ion conducting electrolyte within SOFCs, the onset of significant electronic conduction at low oxygen partial pressures makes solid solutions within the $Zr_{1-y}Y_yO_{2-y/2}$–Y_3NbO_7 series of some interest for the role of anode electrode material [19, 20]. The addition of Y_3NbO_7 to pure ZrO_2 (corresponding to the $y = 0$ system, i.e. $Zr_{1-x}Y_{0.75x}Nb_{0.25x}O_{2-x}$), stabilizes the c* phase for $x \gtrsim 0.25$, with the highest ionic conductivity observed close to this composition as in the binary doped zirconias [21]. Two further systems which have been investigated are $Zr_{0.85-0.85x}Y_{0.15+0.6x}Nb_{0.25x}O_{1.93-0.18x}$, which joins Y_3NbO_7 with the $Zr_{1-y}Y_yO_{2-y/2}$ compound whose yttrium content ($y = 0.15$) has the highest conductivity [22, 23] and $Zr_{0.5-0.5x}Y_{0.5+0.25x}Nb_{0.25x}O_{1.75}$, in which the zirconia-rich end member has composition $Zr_2Y_2O_7$ (i.e. $y = 0.5$) [22, 24, 25].

The $Zr_{0.5-0.5x}Y_{0.5+0.25x}Nb_{0.25x}O_{1.75}$ solid solution is of particular interest because the oxygen (and, hence, vacancy) concentration is constant across the series, allowing the role of the cation sublattice on the conducting and structural properties to be probed. As discussed by Irvine *et al* [26], Nb^{5+} dopant ions are (effectively) oppositely charged with respect to Y^{3+} and have a smaller ionic radius. Thus, the addition of Nb^{5+} might be expected to reduce both the vacancy association effects and strain within the lattice and, as a consequence, increase the ionic conductivity. However, impedance spectroscopy measurements indicate that the conductivity decreases as x increases [20, 25]. Conversely, from the structural viewpoint, neutron diffraction studies show that the isotropic thermal vibration parameter of the anions (which essentially models the level of static disorder within the O^{2-} sublattice) increases with x [20]. Electron diffraction and transmission electron microscopy (TEM) studies have suggested that the anion vacancies are aligned in pairs along the ⟨111⟩ directions within the $x = 1$ (Y_3NbO_7) composition, in manner related to the pyrochlore structure, but in ⟨110⟩ directions at the $x = 0$ ($Zr_2Y_2O_7$) end, which resembles the situation within the C-type structure of Y_2O_3 [24]. This implies that short-range vacancy ordering of the type observed in the pyrochlore structure is more favourable to anion mobility than the C-type arrangement [23], though no clear explanation of this structure–property relationship has been provided to date.

In this paper we report the results of a combined impedance spectroscopy, neutron diffraction and computer simulation study of the system $Zr_{0.5-0.5x}Y_{0.5+0.25x}Nb_{0.25x}O_{1.75}$ with $0 \leqslant x \leqslant 1$. The former technique confirms earlier reports that the ionic conductivity decreases significantly with x [20, 25], whilst the diffraction studies include analysis of the 'total' (i.e. Bragg and diffuse) scattering to investigate changes in the short-range correlations between ions as a function of x and how these relate to the anion conductivity. The computer simulations successfully reproduce the experimentally determined short-range ionic correlations and the composition dependence of the ionic conductivity. This provides an explanation for the apparently conflicting evidence for increased lattice disorder and decreased ionic conductivity with increasing x in the $Zr_{0.5-0.5x}Y_{0.5+0.25x}Nb_{0.25x}O_{1.75}$ system.

2. Experimental methods

2.1. Sample preparation

Powder samples of $Zr_{0.5-0.5x}Y_{0.5+0.25x}Nb_{0.25x}O_{1.75}$ with $x = 0.0$, 0.2, 0.4, 0.6, 0.8 and 1.0 of typical volumes of 2.5 cm^3 were prepared by mixing stoichiometric amounts of the previously dried binary oxides Y_2O_3, Nb_2O_5 and ZrO_2 supplied by the Aldrich Chemical Company and of stated purities 99.999%, 99.99% and 99.99%, respectively. Each sample mixture was thoroughly ground for about 1 h and thereafter heated to 1823 K for 24 h before being pressed to pellets that were heated for another 48 h at 1823 K. Samples used for neutron diffraction were subsequently crushed and ground into a fine powder. After the neutron diffraction experiment the samples were re-sintered to pellets at 1773 K and used for the impedance spectroscopy studies.

2.2. Impedance spectroscopy

Two point AC conductivity measurements of the ionic conductivity were performed using pelleted samples of approximate dimensions 10 mm diameter and 1.5 mm height. These were held between spring-loaded platinum disks inside a ProboStat cell supplied by NorECs and heated from 773 to 1473 K in steps of 10 K under an atmosphere of air. Complex impedance measurements were performed using a Solartron SI 1260 Frequency Response Analyser over the frequency range from 1 Hz to 1 MHz, with the real component of the sample impedance and, hence, the total conductivity, determined by least-squares equivalent circuit fitting to the frequency dependent data using the program ZVIEW.

2.3. Neutron powder diffraction and total scattering

The neutron powder diffraction experiments were performed on the Polaris powder diffractometer at the ISIS facility, Rutherford Appleton Laboratory, UK [27] with the sample encapsulated inside a thin-walled vanadium can of ∼6 mm diameter and ∼60 mm height. The diffraction data were collected for approximately 12 h and the models of the averaged structure determined using the GSAS software [28]. For the total scattering study, the measured neutron diffraction data was corrected for the effects of background scattering from the sample environment and beam attenuation using the program Gudrun [29], which also puts the scattered intensity onto the absolute scattering cross-section scale required for subsequent modelling. The normalized total scattering structure factors, $S(Q)$, were then used to obtain the corresponding total radial distribution functions, $G(r)$, via a Fourier transform

$$G(r) = \frac{1}{(2\pi)^3\rho_0}\int_0^\infty 4\pi Q^2 S(Q)\frac{\sin Q_r}{Q_r}\,\mathrm{d}Q, \qquad (1)$$

where ρ_0 is the average atom number density (in atoms Å^{-3}). $G(r)$ can also be written as a sum of the individual partial radial distribution functions, $g_{ij}(r)$, weighted by the concentrations of the two species, c_i and c_j and their neutron scattering lengths, b_i and b_j, so that

$$G(r) = \sum_{i,j=1}^{n} c_i c_j \bar{b}_i \bar{b}_j g_{ij}(r) \Big/ \left(\sum_{i=1}^{n} c_i \bar{b}_i\right)^2. \qquad (2)$$

The partial radial distribution functions are given by

$$g_{ij}(r) = \frac{1}{4\pi r^2\,\mathrm{d}r}\frac{n_{ij}(r)}{\rho_j}, \qquad (3)$$

where $n_{ij}(r)$ is the number of particles of type j located at a distance between r and $r+\mathrm{d}r$ from a particle of type i and ρ_j is the number density of particles of type j, given by $\rho_j = c_j\rho_0$.

2.4. Reverse Monte Carlo modelling

Analysis of the total neutron scattering data (Bragg peaks plus diffuse scattering components) was performed using the RMCProfile software [30] which uses the reverse Monte Carlo (RMC) method [31, 32]. Each RMC simulation used a configuration box of 10 × 10 × 10 unit cells, i.e. containing a total of 4000 cations (Y, Nb and Zr atoms according to sample stoichiometry) and 7000 oxygen atoms. All atoms in each RMC configuration box were initially randomly distributed over their regular cation and anion crystallographic positions in the fluorite structure, i.e. space group $Fm\bar{3}m$ with the cations at the 4(a) 0, 0, 0 site and the oxygen atoms distributed over the 8(c) 1/4, 1/4, 1/4 site. These initial configurations were subsequently improved using the soft bond valence sum (BVS) constraint within the RMCProfile code [33] (without any experimental data) until approximately 30 000 accepted moves were generated. The ensuing RMC simulations were fitted using the reciprocal space data, $S(Q)$ and the real space data, $G(r)$, plus the Bragg profile data which provides the constraint of long-range crystallinity. The former is broadened by convolution with a box function to reflect the finite size of the simulation box, where

$$S_{\mathrm{box}}(Q) = \frac{1}{\pi}\int_{-\infty}^{\infty} S_{\mathrm{expt}}(Q')\frac{\sin L(Q-Q')/2}{Q-Q'}\,\mathrm{d}Q. \qquad (4)$$

L is the smallest dimension of the RMC configuration and, as such, defines the upper limit of $G(r)$.

The RMC simulations also made use of the BVS constraint [33] and a closest approach constraint that proved important to avoid short O–O contacts. The former helps to differentiate between the cation species within the fitting procedure, since all have rather similar neutron scattering lengths ($b_{\mathrm{Y}} = 7.750\times10^{-15}$ m, $b_{\mathrm{Nb}} = 7.054\times10^{-15}$ m and $b_{\mathrm{Zr}} = 7.160\times10^{-15}$ m). The quality of the final fit to both the $S_{\mathrm{box}}(Q)$ and the $G(r)$ for the Y_3NbO_7 and $Zr_2Y_2O_7$ end members is shown in figures 2 and 3, respectively. None of the RMC simulations of the $Zr_{0.5-0.5x}Y_{0.5+0.25x}Nb_{0.25x}O_{1.75}$ samples provides any evidence for short-range or long-range cation ordering, i.e. the use of cation swapping neither improved the agreement with experimental data or indicated any tendency for a particular cation species to be surrounded preferentially by cations of the same or a different kind. This was additionally confirmed with total scattering data collected for the isostructural compound Yb_3NbO_7, using the same experimental conditions described above. The greater difference in neutron scattering length between Yb and Nb ($b_{\mathrm{Yb}} = 12.430\times10^{-15}$ m) significantly increases the sensitivity to cation ordering effects, but none were observed.

3. Molecular dynamic simulations

Two different models have been optimized for the molecular dynamics (MD) simulations of the $Zr_{0.5-0.5x}Y_{0.5+0.25x}Nb_{0.25x}O_{1.75}$ system. The first is an aspherical ion model that includes quadrupole polarization (QUAIM) and the second is a simpler dipole polarizable ion model (DIPPIM). In both cases, all ions carry their formal (valence) charges. The other parameters in these models are obtained by a generalized 'force-matching' procedure to the results of condensed-phase *ab initio* DFT calculations as described in the appendix. The models themselves are briefly described below.

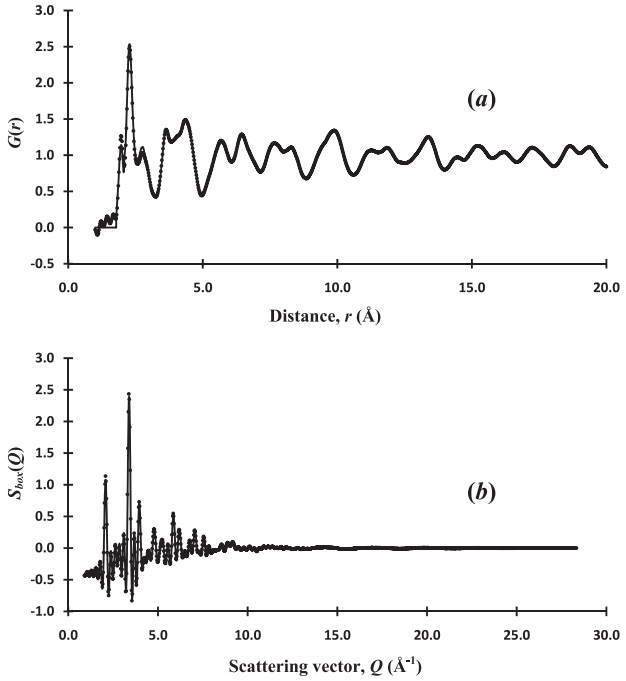

Figure 2. The (*a*) $G(r)$ and (*b*) $S_{\rm box}(Q)$ fits obtained by the RMC simulation of the neutron diffraction data from Y_3NbO_7, with dots showing the experimental data and the solid line showing the calculated profile.

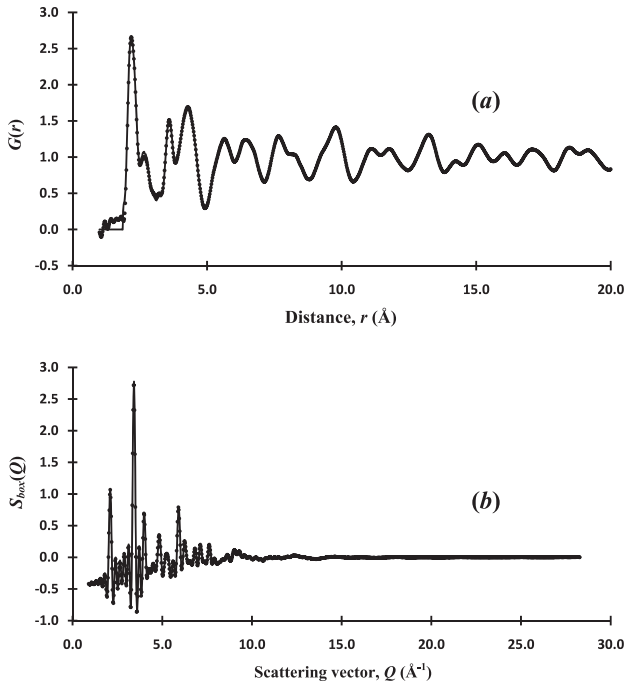

Figure 3. The (*a*) $G(r)$ and (*b*) $S_{\rm box}(Q)$ fits obtained by the RMC simulation of the neutron diffraction data from $Zr_2Y_2O_7$, with dots showing the experimental data and the solid line showing the calculated profile.

3.1. Quadrupolar aspherical ion model (QUAIM)

The parameterization of the polarizable ion model for the $Zr_{0.5-0.5x}Y_{0.5+0.25x}Nb_{0.25x}O_{1.75}$ system is very similar to that used previously by Jahn *et al* [34, 35]. As a result, only a brief summary will be given here. The interionic potential is constructed from four components, describing charge–charge, dispersion, overlap repulsion and polarization effects. The first two components are purely pairwise additive, so that

$$V^{qq} = \sum_{i \leqslant j} \frac{q_i q_j}{r_{ij}}, \tag{5}$$

where q_i is the formal charge for ion i. The dispersion interactions include dipole–dipole and dipole–quadrupole terms

$$V^{\rm disp} = \sum_{i \leqslant j} \left[\frac{f_6^{ij}(r^{ij}) c_6^{ij}}{r_{ij}^6} + \frac{f_8^{ij}(r^{ij}) c_8^{ij}}{r_{ij}^8} \right], \tag{6}$$

with c_6^{ij} and c_8^{ij} as the dipole–dipole and dipole–quadrupole dispersion coefficients, respectively and f_n^{ij} as the Tang–Tonnies dispersion damping function, describing short-range corrections to the asymptotic dispersion term.

For the short-range repulsive terms of the potential, deformable oxygen ions and rigid cations are considered. The repulsion between the small cations is neglected, as previously [35, 36]. The shape deformations are taken as relatively insignificant for the anion–anion repulsions, which are therefore represented by simple Born–Mayer exponentials, but they are substantial in the shell of nearest neighbours, i.e. for the anion–cation repulsion. The expression used here for the short-range repulsion is thus given by

$$\begin{aligned} V^{\rm rep} = {} & \sum [A^{+-} {\rm e}^{-a^{+-} \varrho^{ij}}] + \sum [A^{--} {\rm e}^{-a^{--} r^{ij}}] \\ & + \sum [B^{+-} {\rm e}^{-b^{+-} r_{ij}^2}] + \sum [B^{--} {\rm e}^{-b^{--} r_{ij}^2}] \\ & + \sum D({\rm e}^{\beta \delta \sigma^i} + {\rm e}^{-\beta \delta \sigma^i}) + ({\rm e}^{\zeta^2 |\nu^i|^2} - 1) \\ & + ({\rm e}^{\eta^2 |\kappa^i|^2} - 1), \end{aligned} \tag{7}$$

where $\varrho^{ij} = r^{ij} - \delta\sigma^i - S_\alpha^{(1)} \nu_\alpha^i - S_{\alpha\beta}^{(2)} \kappa_{\alpha\beta}^i$ and a summation of repeated indices is implied. The variable $\delta\sigma^i$ characterizes the deviation of the radius of oxide ion i from its default value, while ν_α^i is a set of three variables describing the Cartesian components of a dipolar distortion of the ion and $\kappa_{\alpha\beta}^i$ is a set of five independent variables describing the corresponding quadrupolar shape distortions. In the expression for the short-range repulsion, $|\kappa|^2 = \kappa_{xx}^2 + \kappa_{yy}^2 + \kappa_{zz}^2 + 2(\kappa_{xy}^2 + \kappa_{xz}^2 + \kappa_{yz}^2)$, and $S_\alpha^{(1)} = (r_\alpha^{ij})/r^{ij}$ plus $S_{\alpha\beta}^{(2)} = 3(r_\alpha^{ij} r_\beta^{ij})/(r^{ij})^2 - \delta_{\alpha\beta}$ are the interaction tensors. The last summation includes the self-energy terms, representing the energy required to deform the anion charge density, with β, ζ and κ as effective force constants. The extent of each ion's distortion is determined at each MD time step by energy minimizations. The terms $\sum [B^{+-} {\rm e}^{-b^{+-} r_{ij}^2}]$ and $\sum [B^{--} {\rm e}^{-b^{--} r_{ij}^2}]$ are Gaussians which act as a steep repulsion wall and account for the anion hard core. These extra terms are used in cases where the ions are strongly polarized to avoid instability problems at very small anion–cation separations [37].

The polarization part of the potential incorporates dipolar and quadrupolar contributions as described by equation (2.5)

in [38]. The instantaneous values of these moments are obtained by minimization of this expression. The charge-dipole and charge-quadrupole cation–anion and anion–anion asymptotic functions include terms which account for penetration effects at short-range by using Tang–Tonnies damping functions of the form

$$g_{\mathrm{D}}(r^{ij}) = c_{\mathrm{D}} \mathrm{e}^{-b_{\mathrm{D}} r^{ij}} \sum_{k=0}^{4} \frac{(b_{\mathrm{D}} r^{ij})^k}{k!} \tag{8}$$

and

$$g_{\mathrm{Q}}(r^{ij}) = c_{\mathrm{Q}} \mathrm{e}^{-b_{\mathrm{Q}} r^{ij}} \sum_{k=0}^{6} \frac{(b_{\mathrm{Q}} r^{ij})^k}{k!}. \tag{9}$$

D and Q represent the dipolar and quadrupolar parts, respectively. The parameters b_{D} and b_{Q} determine the range at which the overlap of the charge densities affects the induced multipoles, whilst the parameters c_{D} and c_{Q} determine the strength of the ion response to this effect.

3.2. Dipole-polarizable ion model (DIPPIM)

The model described above has the drawback of being computationally very demanding. The studies presented in this paper require long simulations, with many hundreds of ions. For this reason, alternative (faster) potentials have also been developed where the ion-shape deformation effects and quadrupolar contributions to the polarization part of the potential are neglected. As shown in section 4.3, omitting the short-range deformation and quadrupole polarization terms leads to a slightly poorer agreement between simulated and experimental structures but allows much longer simulations to obtain good statistics for the conduction properties. In this case, the short-range repulsion term is given by [37, 39],

$$V^{\mathrm{rep}} = \sum \left[\frac{A^{+-} \mathrm{e}^{-a^{+-} r^{ij}}}{r_{ij}} \right] + \sum \left[\frac{A^{--} \mathrm{e}^{-a^{--} r^{ij}}}{r_{ij}} \right] + \sum [B^{+-} \mathrm{e}^{-b^{+-} r_{ij}^2}] + \sum [B^{--} \mathrm{e}^{-b^{--} r_{ij}^2}], \tag{10}$$

where the $1/r$ form was selected as this is known to give a better fit of the short-range interaction [37]. The polarization part of the potential is equal to equation (2.5) in [38] with C^i and B^i set equal to zero. See the appendix for further details regarding the parameters used for both the QUAIM and DIPPIM models.

3.3. MD simulation details

All the simulations on the $Zr_{0.5-0.5x}Y_{0.5+0.25x}Nb_{0.25x}O_{1.75}$ system were performed using a cubic simulation box with $4 \times 4 \times 4$ unit cells, i.e. 256 cations and 448 oxygen ions. The cation species were randomly distributed over the cation sublattice, since there is no experimental evidence of any ordering (see section 2.4 and [20, 21, 25]). The time step used was 20 au $= 4.84 \times 10^{-4}$ ps and all the runs were performed at constant pressure and temperature (NPT ensemble), with thermostats and barostats as described elsewhere [40, 41] and the external pressure set to zero. Only the high temperature runs were performed at constant volume and temperature (NVT ensemble), in which the cell volume was obtained from a previous run in a NPT ensemble. Coulombic and dispersion interactions were summed using Ewald summations while the short-range part of the potential was truncated to half the length of the simulation box, i.e., about 19 au. The potential used was the full QUAIM model for the calculation of the $G(r)$s, whilst the DIPPIM potential was used to calculate the diffusion coefficients and ionic conductivities.

The simulations were started from a perfect fluorite structure and the system was equilibrated at 2000 K for 50 000 steps, to allow both cations and anions to relax in the crystal. The system was then cooled down, first to 1000 K for 10 000 steps and then to 300 K for another 10 000 steps, before a final run of 10 000 steps was performed to accumulate sufficient statistics for the calculation of the radial distribution functions. Ionic conductivities were estimated from the simulations using the formula

$$\sigma = \frac{c^2 \rho D}{k_{\mathrm{B}} T}, \tag{11}$$

where c is the charge of the mobile species (in this case the oxygen ions), ρ is the system density, D is the diffusion coefficient, k_{B} is the Boltzmann constant and T is the temperature. The diffusion coefficient can be obtained from the slope of the mean squared displacement at long times, i.e.

$$D = \lim_{t \to \infty} \frac{1}{6 N_{\mathrm{O}^{2-}}} \left\langle \sum_{j=1}^{N_{\mathrm{O}^{2-}}} [\boldsymbol{r}_j(t) - \boldsymbol{r}_j(0)]^2 \right\rangle, \tag{12}$$

where $N_{\mathrm{O}^{2-}}$ is the number of oxygen ions and $\boldsymbol{r}_j(t)$ is the position of ion j at time t.

The calculations of the diffusion coefficient were performed using the same configuration of ions as used in the calculation of the $G(r)$. This was then equilibrated for 100 000 steps at the required temperature in an NPT ensemble and then in a longer simulation of up to 1000 000 steps, i.e. 484 ps, using an NVT ensemble to accumulate sufficient statistics for the calculation of the mean squared displacements.

4. Results

4.1. Ionic conductivity measurements

The ionic conductivity, σ, of the $Zr_{0.5-0.5x}Y_{0.5+0.25x}Nb_{0.25x}O_{1.75}$ samples with $x = 0.0, 0.2, 0.4, 0.6, 0.8$ and 1.0, measured at $T = 1473$ K, are shown in figure 4(*a*). The overall decrease in σ with increasing x is consistent with the trends observed previously by Irvine *et al* [20] and by Lee *et al* [21, 25]. The slightly lower ionic conductivities obtained in this work are probably a consequence of sample pellets with a more porous structure.

4.2. Rietveld refinement of the averaged structure

Rietveld refinement [42] of the neutron powder diffraction data collected from the six samples of $Zr_{0.5-0.5x}Y_{0.5+0.25x}Nb_{0.25x}O_{1.75}$ with $x = 0.0, 0.2, 0.4, 0.6, 0.8$ and 1.0 were performed using the conventional model for an anion-deficient fluorite structure, with the cations (Y, Nb and Zr) randomly distributed over the 4(a) sites of space group $Fm\bar{3}m$ and the anions

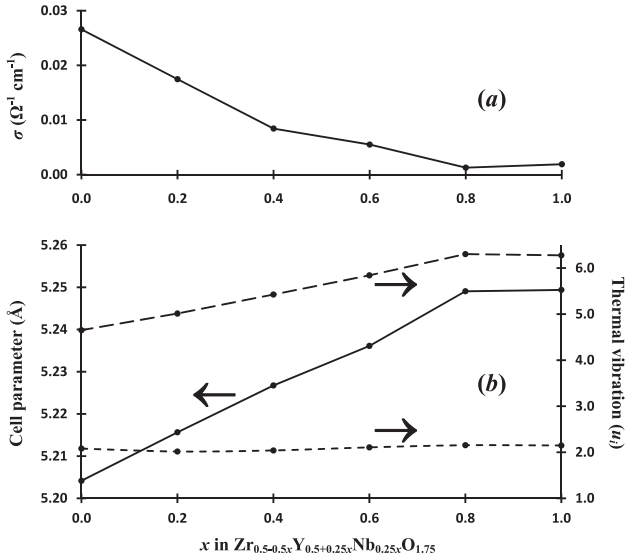

Figure 4. (*a*) Measured conductivity (at 1473 K), and (*b*) changes in the unit cell parameters (solid line), cation thermal vibration (short dashed line) and anion thermal vibration (long dashed line) for the $Zr_{0.5-0.5x}Y_{0.5+0.25x}Nb_{0.25x}O_{1.75}$ samples. The standard uncertainties, for all data points, are smaller than the size of the symbol.

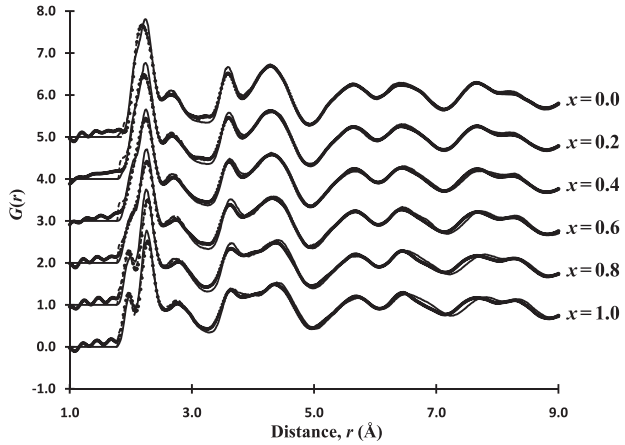

Figure 5. Total radial distribution functions, $G(r)$, from the QUAIM (solid line) and the RMC (dashed line) simulations for the $Zr_{0.5-0.5x}Y_{0.5+0.25x}Nb_{0.25x}O_{1.75}$ system. The black dots represent the $G(r)$ obtained directly by Fourier transform of the experimental total scattering structure factor, $S(Q)$.

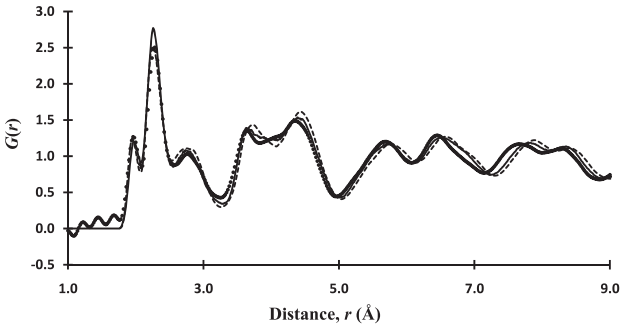

Figure 6. The simulated total radial distribution functions, $G(r)$, obtained for Y_3NbO_7 using the QUAIM model (solid line) and the DIPPIM model (dashed line). The black dots represent the $G(r)$ obtained directly by Fourier transform of the experimental total scattering structure factor, $S(Q)$.

distributed over the 8(c) sites at 1/4, 1/4, 1/4, etc, with an average occupancy of 7/8, The refined parameters comprised a scale factor, the cubic lattice parameter, a, isotropic thermal vibration parameters for the cations and anions, u_M and u_O, plus 20 coefficients of a shifted Chebyshev polynomial describing the undulating background scattering and four coefficients describing Gaussian and Lorentzian contributions to the Bragg peak shapes. Excellent fits to the experimental data were obtained in all cases using the adopted structural model. Alternative models, allowing the cations or anions to displace preferentially in the ⟨100⟩, ⟨110⟩ or ⟨111⟩ directions, did not improve the quality of the fit. The variation of a, u_M and u_O, with x is illustrated in figure 4(*b*), with the unit cell constant for the Y_3NbO_7 and $Zr_2Y_2O_7$ end members being almost the same, 5.249 37(4) Å and 5.204 14(9) Å, respectively. The changes in thermal vibration parameters are also small for the cations, whilst the anion thermal vibration parameter increases significantly with increasing x, as seen previously [20].

4.3. G(r)s from RMC and MD simulations

The total radial distribution functions, $G(r)$, for all the $Zr_{0.5-0.5x}Y_{0.5+0.5x}Nb_{0.25x}O_{1.75}$ compositions obtained from both the RMC and the MD simulations agree well with each other and with the experimental $G(r)$ obtained by direct Fourier transformation of the total scattering structure factor, $S(Q)$ (see figure 5). Indeed, the almost perfect agreement between the RMC simulation and the experimental data makes them almost indistinguishable. It should be emphasized that the good agreement between the QUAIM model and the experimental data across the entire $Zr_{0.5-0.5x}Y_{0.5+0.25x}Nb_{0.25x}O_{1.75}$ series indicates that the potentials are highly transferable with excellent reproduction of the cation–anion distances and predicted lattice parameters, which agree with the experimental ones to within ±0.5%.

Nonetheless, the MD simulations make use of two different models and the total $G(r)$ obtained with both the QUAIM and the DIPPIM potentials for Y_3NbO_7 are compared with the experimental $G(r)$ in figure 6. The DIPPIM model gives a good fit, though slightly inferior to that given by the QUAIM model, even though it neglects ion-shape deformation effects and quadrupolar interactions. Because the DIPPIM is simpler and faster than the QUAIM we will use it to study the dynamical properties with the reassurance that the predicted structure is not substantially poorer.

4.4. Ionic conductivities from MD simulations

Calculations of the mean square displacements of the ionic species in $Zr_{0.5-0.5x}Y_{0.5+0.25x}Nb_{0.25x}O_{1.75}$, using the DIPPIM model, clearly demonstrate that the oxygen ions are mobile, whilst the cations show no diffusive behaviour. Figure 7 plots $\log \sigma T$ as a function of reciprocal temperature for $Zr_2Y_2O_7$, to

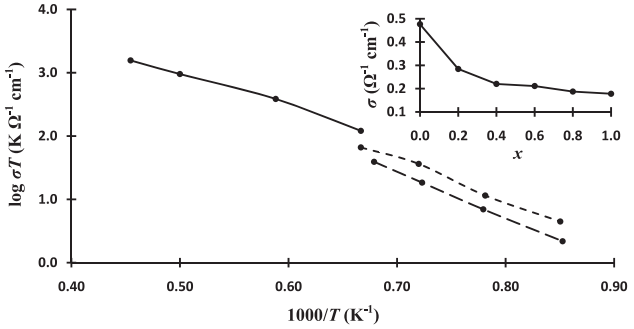

Figure 7. Comparison between the measured conductivity data of Lee *et al* [25] (short dashed line), our experimental data (long dashed line) and the DIPPIM simulations (solid line) for $Zr_2Y_2O_7$. The inset shows changes in the MD simulated conductivity at 2000 K as a function of x in $Zr_{0.5-0.5x}Y_{0.5+0.25x}Nb_{0.25x}O_{1.75}$.

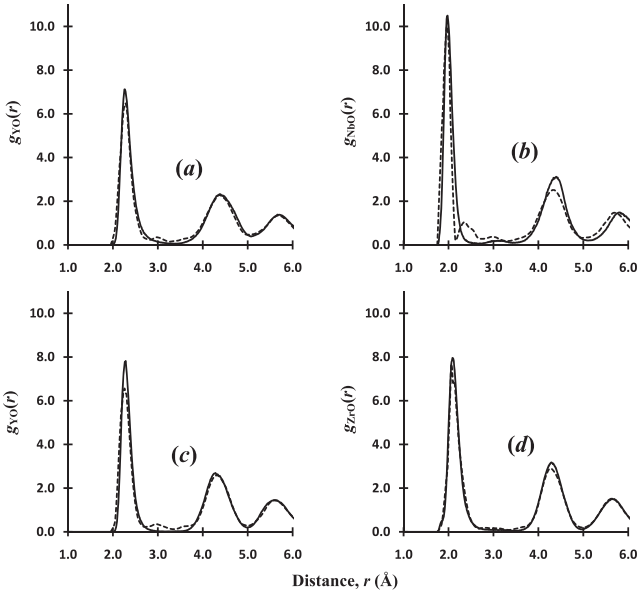

Figure 8. Partial radial distribution functions, $g_{jk}(r)$, as determined from RMC (dashed lines) and QUAIM (solid lines) simulations. (*a*) $g_{YO}(r)$ and (*b*) $g_{NbO}(r)$ are for Y_3NbO_7, whilst (*c*) $g_{YO}(r)$ and (*d*) $g_{ZrO}(r)$ are for $Zr_2Y_2O_7$.

compare the ionic conductivity from the DIPPIM simulations with that published by Lee *et al* [25] and reported here for our samples. The simulations were performed at 1500, 1700, 2000 and 2200 K, since the slow dynamics at lower temperatures would require extremely long simulations in order to obtain a meaningful mean square displacement curve from which a diffusion coefficient can be extracted. The agreement between the experimental and simulated ionic conductivities is quite good, with the differences probably caused by the density of the sample pellets being less than 100% and/or the assumption of uncorrelated motion of the charge carriers which is inherent in equation (11). Nevertheless, the Arrhenius activation energy of 1.1 eV extracted from the simulations is comparable with previous experimental data [25]. The inset to figure 7 shows the calculated bulk ionic conductivity of $Zr_{0.5-0.5x}Y_{0.5+0.25x}Nb_{0.25x}O_{1.75}$ for $x = 0.0$, 0.2, 0.4, 0.6, 0.8, 1.0 at $T = 2000$ K and clearly shows that the conductivity increases with decreasing x, which is also consistent with both our own impedance experiments and earlier work by Lee *et al* [21, 25].

5. Discussion

5.1. Radial distribution functions

The partial radial distribution functions, $g_{jk}(r)$, are readily extracted from the RMC and MD configurations and the resulting partial radial distribution functions, $g_{YO}(r)$, $g_{NbO}(r)$ and $g_{ZrO}(r)$ are shown in figure 8 and compared with those from the QUAIM simulations. The location of the first peak is observed at around 2.28, 1.96 and 2.10 Å for Y–O, Nb–O and Zr–O, respectively, and these differences in bond distances are consistent with the ionic radii reported by Shannon [43]. Interestingly, the bond distances for Y–O and Zr–O given by the simulations imply an oxygen coordination number of between 6 and 7, whilst the Nb–O bond distance suggests an oxygen coordination number slightly lower than 6. The cation–O bond distances given by the Rietveld refinement of the neutron diffraction data for Y_3NbO_7 and $Zr_2Y_2O_7$ are 2.273 05(1) Å and 2.253 46(3) Å, respectively, which are closest to the bond distance for Y–O. The difference between the Nb–O bond distance on a local scale and that expected for a long-range ordered (perfect) fluorite lattice indicates that the addition of Nb^{5+} cations leads to an increase in the degree of short-range disorder within the anion sublattice.

A complete discussion of the local lattice disorder within the $Zr_{0.5-0.5x}Y_{0.5+0.25x}Nb_{0.25x}O_{1.75}$ system must also consider the anion–anion interactions. Figure 9 plots the $g_{OO}(r)$ for all the $Zr_{0.5-0.5x}Y_{0.5+0.25x}Nb_{0.25x}O_{1.75}$ compositions obtained using the RMC and QUAIM simulations. It is clear in figure 9(*a*) that the position of the first O–O radial distribution peak for the $Zr_{0.5-0.5x}Y_{0.5+0.25x}Nb_{0.25x}O_{1.75}$ samples is shifted towards a shorter distance in comparison with Y_3NbO_7 (see table 1). The first $g_{OO}(r)$ peak position for $Zr_2Y_2O_7$ is closer to the expected value for a fluorite structure of similar unit cell size, as illustrated by the plot of the $g_{OO}(r)$ for a perfect fluorite in figure 9(*b*). However, the shift from the expected distance increases with increasing Nb content, which clearly indicates that the extent of disorder within the oxygen sublattice is highest in the Y_3NbO_7 end member, but decreases towards the $Zr_2Y_2O_7$ end member. Further evidence of the increased disorder within the anion sublattice with x is the existence of a more pronounced second peak at around 3.55 Å in the plotted $g_{OO}(r)$s for $Zr_2Y_2O_7$, clearly indicating that $Zr_2Y_2O_7$ retains a more regular cubic arrangement of anions around its cations, whilst the local anion arrangement within Y_3NbO_7 is rather more distorted on a local scale. This explains the increase in the oxygen thermal vibration parameter, u_O, with x shown by the refinements of the neutron diffraction data (figure 4(*b*)), since u_O effectively models the broader distribution of anions around their ideal 8(c) sites.

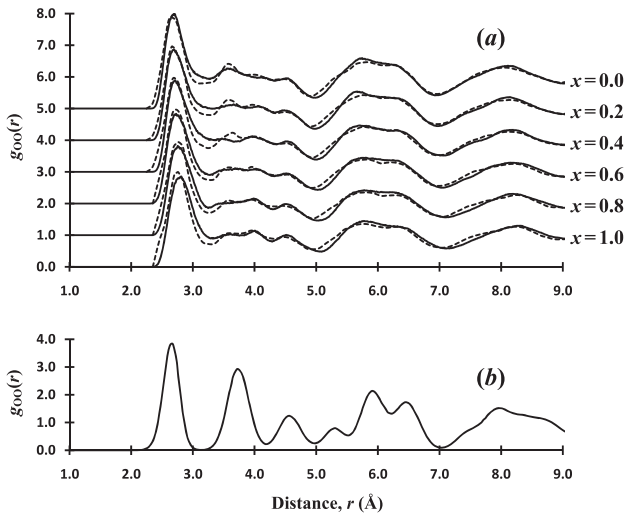

Figure 9. (*a*) The partial radial distribution functions, $g_{OO}(r)$ for the $Zr_{0.5-0.5x}Y_{0.5+0.25x}Nb_{0.25x}O_{1.75}$ system, calculated from both the RMC model (dashed line) and the QUAIM simulations (solid line). (*b*) The corresponding $g_{OO}(r)$ expected for a perfect fluorite structure scaled to the unit cell size of Y_3NbO_7.

Table 1. Comparison of the position of the first peak $g_{OO}(r)$ with that expected from Rietveld refinement of the neutron diffraction data.

Compound	Position of first $g_{OO}(r)$ peak (Å)	Shift from expected[a] (Å)
Y_3NbO_7	2.76	0.13
$Zr_{0.4}Y_{2.8}Nb_{0.8}O_7$	2.78	0.15
$Zr_{0.8}Y_{2.6}Nb_{0.6}O_7$	2.74	0.12
$Zr_{1.2}Y_{2.4}Nb_{0.4}O_7$	2.70	0.09
$Zr_{1.6}Y_{2.2}Nb_{0.2}O_7$	2.68	0.07
$Zr_2Y_2O_7$	2.66	0.06

[a] Based on Rietveld refinement.

5.2. Angular distribution functions

In the ideal cubic fluorite structure the cations are situated at the centre of a cube of anions and the expected O–cation–O bond angles are 70.5°, 109.5° and 180°, corresponding to anion pairs that are nearest neighbours along the ⟨100⟩, ⟨110⟩ or ⟨111⟩ directions, respectively. Figure 10 plots the angular distribution functions, $A_{O\text{cation}O}(\theta)$, obtained from both the RMC and the MD simulations. The cases of $A_{OYO}(\theta)$ and $A_{OZrO}(\theta)$ show broad peaks centred at the expected angles, whilst the $A_{ONbO}(\theta)$ angular distributions are shifted towards bond angles distributed around 85°–95° and 180°. The Nb–O pair distribution function described above indicates that the Nb^{5+} is coordinated to around 6 surrounding oxygen atoms, as opposed to 7 for Y and Zr. These observations suggest that the Nb^{5+} cation is attempting to adopt a distorted octahedral geometry of surrounding anions, of the type found in several phases of Nb_2O_5 [44, 45].

The increasing short-range disorder in the $Zr_{0.5-0.5x}Y_{0.5+0.25x}Nb_{0.25x}O_{1.75}$ system with increasing x is, therefore, a consequence of the Nb^{5+} cation's desire to adopt its preferred octahedral coordination, with substantially shorter bond distances than the average cation–O bond distance within

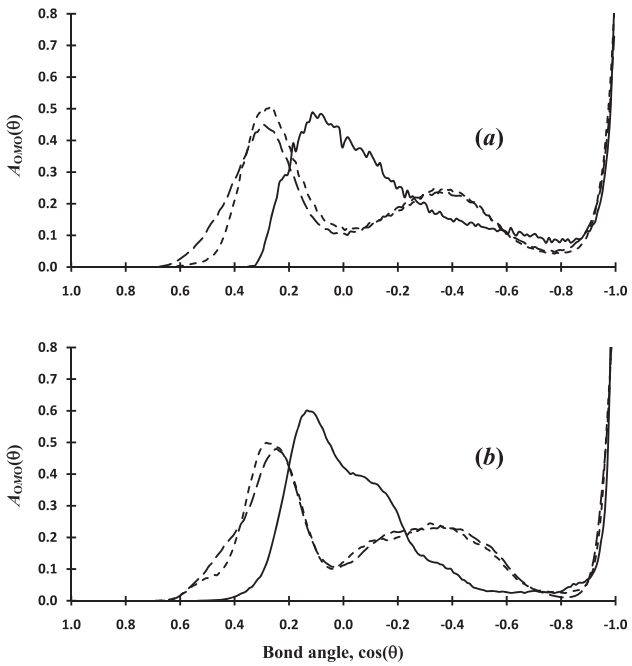

Figure 10. The calculated angular distribution functions, $A_{OYO}(\theta)$ (long dashed line), $A_{OZrO}(\theta)$ (short dashed line) and $A_{ONbO}(\theta)$ (solid line), from both (*a*) RMC and (*b*) QUAIM simulations.

the material (as given by the Rietveld refinement of the Bragg scattering). The lower anion coordination number for Nb^{5+} and more distorted O–cation–O bond angles around the Nb^{5+} generate vacant anion sites that are randomly distributed within the lattice (since there is no cation ordering) and might be expected to increase the ionic conductivity. However, this is not the case and it is necessary to consider the mobility of individual anions.

5.3. Oxygen mobility

A detailed investigation of the mean squared displacements of the individual anions within the MD simulations of Y_3NbO_7 indicated that a relatively small number of anions possess a very high mobility, but also that a significant anion fraction do not take part in the conducting process at all. To illustrate this behaviour and allow a comparison with the case of $Zr_2Y_2O_7$, the DIPPIM simulations were divided into 10 steps of equal time (∼48.4 ps) in order to compare the mobility of different anions. Each anion moving a distance greater than λ (with λ equal to 1.5 times the average mean square displacement of an anion) is assigned to be 'mobile'. In both Y_3NbO_7 and $Zr_2Y_2O_7$, λ was comparable to the nearest neighbour O–O separation. Thus, it is possible to obtain the distribution of 'mobility' for the anions in Y_3NbO_7 and $Y_2Zr_2O_7$, with a maximum value of 10 and a minimum value of 0. As illustrated in figure 11, the main difference in the anion mobility behaviour between Y_3NbO_7 and $Zr_2Y_2O_7$ is that the former has a large fraction of 'immobile' anions that do not contribute to the overall anion conductivity. Conversely, $Zr_2Y_2O_7$ has a broad peak with a maximum at around 2–3 in 'mobility'. The latter suggest that almost all of the anions

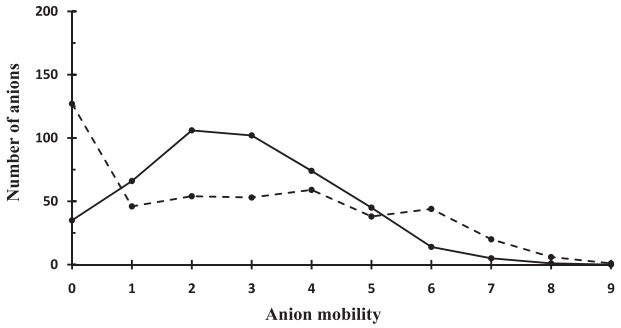

Figure 11. Plot of the number of anions versus anion 'mobility' for Y_3NbO_7 (dashed line) and $Zr_2Y_2O_7$ (solid line), demonstrating the greater mobility of the anions in $Zr_2Y_2O_7$ and the significant fraction of immobile anions in Y_3NbO_7.

contribute to the conductivity in $Zr_2Y_2O_7$ and do not become trapped in a particular anion site.

A detailed analysis of the trapped anions within Y_3NbO_7 reveals that they merely vibrate around their equilibrium position and it is tempting to associate the trapping of O^{2-} anions with their strong Coulombic interaction with Nb^{5+} cations. However, closer inspection shows this assumption to be incorrect, since the majority of trapped anions have surrounding cation environments with a higher than average number of Y^{3+}. So, whilst Y_3NbO_7 has a small number of anions that are very mobile (see figure 11), there are numerous anions trapped at sites with many neighbouring Y^{3+} cations. Thus, increasing x is detrimental to the conductivity process because it increases the concentration of Y^{3+} cations. A plausible explanation of this effect is that the increased ionic size of Y^{3+} (compared to the Zr^{4+} it replaces) effectively traps the O^{2-} anions within their tetrahedral cavities.

6. Conclusions

As a general rule, crystalline ionic solids showing high values of ionic conductivity are characterized by relatively high levels of disorder within the crystal lattice. In this context, the $Zr_{0.5-0.5x}Y_{0.5+0.25x}Nb_{0.25x}O_{1.75}$ system is rather unusual, since the degree of disorder within the anion sublattice, as indicated by the anion thermal vibration parameter determined by neutron powder diffraction studies, increases with x whilst the ionic conductivity decreases with x. The combination of impedance spectroscopy studies, measurements of the total (Bragg plus diffuse) neutron scattering and MD simulations using potentials derived from *ab initio* calculations has provided a plausible model to explain this behaviour. The increased disorder within the anion sublattice as x increases is principally caused by the increased concentration of the smaller Nb^{5+} cations. These pentavalent cations might, in themselves, even promote the anion conduction process, despite their stronger Coulombic interactions. However, this effect is outweighed by the simultaneous increase in the Y^{3+} content with x, since these larger cations act as effective traps for the anions and, overall, the ionic conductivity decreases. Whilst this explanation can successfully account for the observed structural properties and ionic conductivity within the $Zr_{0.5-0.5x}Y_{0.5+0.25x}Nb_{0.25x}O_{1.75}$ system, it does prompt a number of questions. In particular, the role of the size and charge of cations in promoting/hindering anion diffusion needs to be understood, and this issue will be addressed in a future publication. In a wider context, such information is needed to inform attempts to synthesize new compounds possessing high oxide-ion conductivities to meet the expanding demands provided by fuel cell and gas sensor technologies.

Alongside these physical results, the paper has demonstrated a remarkable capability of the RMC analysis of the total neutron scattering for this type of system. Figures 8 and 9 show excellent accord between the partial radial distribution functions extracted from the RMC and the MD simulations, despite the fact that 6 partials contribute to the scattering in the $Zr_2Y_2O_7$ and Y_3NbO_7 systems and that the $g_{OO}(r)$ is strongly affected by disorder. The bond angle distribution functions (figure 10) agree too, which is even more remarkable since the total scattering depends on two-particle correlations, while the bond angle involves the relative position of three particles. Although one should be careful not to confuse the MD system with the real material, the many-body correlations do follow from a physical interaction potential (including many-body interactions) which was parameterized in a non-empirical way and the MD predicted properties agree well with experiment.

Acknowledgments

We wish to thank the EaStCHEM resource computing facility (http://www.eastchem.ac.uk/rcf) for computing resources. DM thanks the EPSRC and the STFC for his PhD funding. STN wishes to thank the EU Research and Technology Development Framework Programme for financial support. The STFC is thanked for allocating beamtime at the ISIS Facility.

Appendix

A.1. DFT reference calculations

Both the QUAIM and DIPPIM interaction models were parameterized by force-matching to DFT calculations carried out on condensed-phase configurations, as described by Jahn *et al* in [34, 35]. Starting from a Born–Mayer potential from the literature [46] for yttria-stabilized zirconia (with the Nb–O interaction obtained by scaling the Zr–O one), one atomic configuration for Y_3NbO_7 and one for ZrO_2 were generated by running short MD simulations on small cells (80–96 ions) at 1500 K. These two configurations were used to run DFT reference calculations (see below) and an initial QUAIM model was fitted to the forces, dipoles and quadrupoles. These potentials were then used to generate more reference MD configurations for Y_3NbO_7 and ZrO_2 at 1500 K. For each of these, the Hellman–Feynman forces acting on individual ions of the simulation cell were calculated using the planewave-DFT code CASTEP [47]. All the calculations used norm-conserving pseudopotentials generated via the OPIUM program and planewave energy cut-offs of 1000 eV and were performed using the generalized gradient approximation

Table A.1. Parameters for the QUAIM potentials with values in au, and short-range parameters only reported for those with a b parameter not equal to zero.

	O–O	Y–O	Zr–O	Nb–O
A^{ij}	0.0	165.19	345.01	159.76
a^{ij}	5.0	1.7586	1.9590	1.7038
B^{ij}	50 000	50 000	50 000	50 000
b^{ij}	0.85	1.2	1.2	1.3
C_6^{ij}	44.0	10	10	5
C_8^{ij}	853.0	200	200	100
b_{disp}^{ij}	1.0	1.5	1.5	1.5
D	0.1616			
ζ	1.168			
α	14.49	4.86	2.67	2.53
β	3.154			
η	14.842			
C	1.5574			
$b_{\text{D}}^{\text{O-O}}$	2.097		$b_{\text{D}}^{\text{O-Zr}}$	1.778
$c_{\text{D}}^{\text{O-O}}$	1.058		$c_{\text{D}}^{\text{O-Zr}}$	1.674
$b_{\text{Q}}^{\text{O-O}}$	2.363		$b_{\text{Q}}^{\text{O-Zr}}$	1.048
$c_{\text{Q}}^{\text{O-O}}$	4.999		$c_{\text{Q}}^{\text{O-Zr}}$	0.645
$b_{\text{D}}^{\text{O-Y}}$	1.811		$b_{\text{D}}^{\text{Y-O}}$	1.810
$c_{\text{D}}^{\text{O-Y}}$	2.285		$c_{\text{D}}^{\text{Y-O}}$	−0.891
$b_{\text{Q}}^{\text{O-Y}}$	1.837		$b_{\text{D}}^{\text{Y-Nb}}$	1.788
$c_{\text{Q}}^{\text{O-Y}}$	1.442		$c_{\text{D}}^{\text{Y-Nb}}$	0.717
$b_{\text{D}}^{\text{O-Nb}}$	1.845		$b_{\text{D}}^{\text{Nb-O}}$	1.845
$c_{\text{D}}^{\text{O-Nb}}$	1.714		$c_{\text{D}}^{\text{Nb-O}}$	−0.523
$b_{\text{Q}}^{\text{O-Nb}}$	1.865		$b_{\text{D}}^{\text{Nb-Y}}$	1.788
$c_{\text{Q}}^{\text{O-Nb}}$	1.203		$c_{\text{D}}^{\text{Nb-Y}}$	3.50

Table A.2. Parameters for the DIPPIM potentials with values in au, and short-range parameters only reported for those with a b parameter not equal to zero.

	O–O	Y–O	Zr–O	Nb–O
A^{ij}	4.97	104.53	55.05	59.108
a^{ij}	22.99	1.389	1.144	1.137
B^{ij}	50 000	50 000	50 000	50 000
b^{ij}	0.85	1.35	1.43	1.53
C_6^{ij}	44	10	10	5
C_8^{ij}	853	200	200	100
b_{disp}^{ij}	1.0	1.5	1.5	1.5
α	13.65	4.73	3.23	3.76
$b_{\text{D}}^{\text{O-O}}$	1.99		$b_{\text{D}}^{\text{O-Zr}}$	1.642
$c_{\text{D}}^{\text{O-O}}$	0.689		$c_{\text{D}}^{\text{O-Zr}}$	1.396
$b_{\text{D}}^{\text{O-Y}}$	1.824		$b_{\text{D}}^{\text{Y-O}}$	1.806
$c_{\text{D}}^{\text{O-Y}}$	2.215		$c_{\text{D}}^{\text{Y-O}}$	−0.455
$b_{\text{D}}^{\text{O-Nb}}$	1.844		$b_{\text{D}}^{\text{Nb-Y}}$	1.805
$c_{\text{D}}^{\text{O-Nb}}$	1.700		$c_{\text{D}}^{\text{Nb-Y}}$	3.50

(GGA) according to the Perdew, Burke and Ernzerhof (PBE) scheme. For the calculation of *ab initio* multipoles, the Kohn–Sham orbitals are localized via a Wannier transformation to construct maximally localized Wannier functions (MLWF). From the localized orbitals, ionic dipoles and quadrupoles were calculated [48].

A.2. Force-matching procedure

The potential parameters are optimized by fitting the forces, dipoles and quadrupoles predicted by the QUAIM and DIPPIM potentials for the reference configurations to the respective results from the DFT calculations. The 6 configurations provide a total of around 2500 data points, comprising three Cartesian force components of each individual ion, three components for the dipole and six components for the quadrupole of each ion. While most of the potential parameters are left as free parameters in the fits, there are some exceptions. In the QUAIM fits, the parameter B^i (hyperpolarizability) was set to zero, as this was not found to significantly affect the quality of the fit. In addition, the C^i parameter (quadrupole polarizability) was found to be very small for the cations and therefore was set to zero. For this reason, the short-range effects on the cation quadrupoles were also neglected.

One problem with DFT calculations is the uncontrolled representation of the dispersion interaction. Although dispersion energies only contribute a tiny fraction to the total energy, they have a considerable influence on transition pressures and, in particular, on the material density and stress tensor. For this reason, the dispersion parameters were not included in the fits, as discussed by Madden *et al* [49], but were added afterwards. The parameters in [34] were used after rescaling with respect to the ionic radii. The Gaussian parameters were also added after the fit, which was then rerun to check that its quality was unchanged [37].

The parameters obtained for the QUAIM and DIPPIM potentials are summarized in tables A.1 and A.2. After fitting such a complicated model with tens of parameters it is useful to check that the derived parameters retain their physical meaning. The oxygen polarizability, for instance, is $\alpha \approx 14$ au which is in good agreement with that used previously [36] and that obtained by extrapolation of *ab initio* calculations on other oxides [50]. In addition, the Y and Zr polarizabilities are in good agreement with the value of 4.05 au in [50] (*ab initio* calculations) and 2.76 au in [8] (experimental dielectric properties), respectively.

References

[1] Etsell T H and Flengas S N 1970 *Chem. Rev.* **70** 339–76
[2] Politova T I and Irvine J T S 2004 *Solid State Ion.* **168** 153–65
[3] Scott H G 1975 *J. Mater. Sci.* **10** 1527–35
[4] Subbarao E C and Ramakrishnan T V 1979 *Fast Ionic Transport in Solids* ed P Vashishta *et al* (New York: Elsevier North-Holland) pp 653–6
[5] Catlow C R A, Chadwick A K, Greaves G N and Moroney L M 1984 *Nature* **312** 601–4
[6] Hohnke D K 1981 *Solid State Ion.* **5** 531–4
[7] Khan M S, Islam M S and Bates D R 1998 *J. Mater. Chem.* **8** 2299–307
[8] Mackrodt W C and Woodrow P M 1986 *J. Am. Ceram. Soc.* **69** 277–80
[9] Stefanovich E V, Shluger A L and Catlow C R A 1994 *Phys. Rev.* B **49** 11560–71
[10] Hull S 2004 *Rep. Prog. Phys.* **67** 1233–314

[11] Goff J P, Hayes W, Hull S, Hutchings M T and Clausen K N 1999 *Phys. Rev.* B **59** 14202–19
[12] Fèvre M, Finel A and Caudron R 2005 *Phys. Rev.* B **72** 104117
[13] Allpress J G and Rossell H J 1979 *J. Solid State Chem.* **27** 105–14
[14] Rooksby H P and White E A D 1964 *J. Am. Ceram. Soc.* **47** 94–6
[15] Rossell H J 1979 *J. Solid State Chem.* **27** 115–22
[16] Sirotinkin V P, Evdokimov A A and Trunov V K 1982 *Russ. J. Inorg. Chem.* **27** 931–3
[17] Lee J-H, Yashima M, Kakihana M and Yoshimura M 1998 *J. Am. Ceram. Soc.* **81** 894–900
[18] Miida R, Sato F, Tanaka M, Naito H and Arashi H 1997 *J. Appl. Crystallogr.* **30** 272–9
[19] Irvine J T S, Fagg D P, Labrincha J and Marques F M B 1997 *Catal. Today* **38** 467–72
[20] Irvine J T S, Feighery A J, Fagg D P and García-Martín S 2000 *Solid State Ion.* **136/137** 879–85
[21] Lee J-H and Yoshimura M 2001 *Solid State Ion.* **139** 197–203
[22] Fagg D P and Irvine J T S 1998 *Ionics* **4** 61–71
[23] García-Martín S, Alario-Franco M A, Fagg D P and Irvine J T S 2005 *J. Mater. Chem.* **15** 1903–7
[24] García-Martín S, Alario-Franco M A, Fagg D P, Feighery A J and Irvine J T S 2000 *Chem. Mater.* **12** 1729–37
[25] Lee J-H and Yoshimura M 1999 *Solid State Ion.* **124** 185–91
[26] Irvine J T S, Gibson I R and Fagg D P 1995 *Ionics* **1** 279–85
[27] Hull S, Smith R I, David W I F, Hannon A C, Mayers J and Cywinski R 1992 *Physica* B **180/181** 1000–2
[28] Larson A C and von Dreele R B 1994 General Structure Analysis System (GSAS) *Los Alamos National Laboratory Report* LAUR 86-748
[29] Soper A K Gudrun—A computer program developed for analysis of neutron diffraction data http://www.isis.rl.ac.uk/disordered/dmgroup_home.htm
[30] Tucker M G, Keen D A, Dove M T, Goodwin A L and Hui Q 2007 *J. Phys.: Condens. Matter* **19** 335218
[31] McGreevy R L and Pusztai L 1988 *Mol. Simul.* **1** 359–67
[32] McGreevy R L 2001 *J. Phys.: Condens. Matter* **13** R877–913
[33] Norberg S T, Tucker M G and Hull S 2009 *J. Appl. Crystallogr.* **42** 179–84
[34] Jahn S, Madden P A and Wilson M 2006 *Phys. Rev.* B **74** 024112
[35] Jahn S and Madden P A 2007 *Phys. Earth Planet. Inter.* **162** 129–39
[36] Wilson M, Schonberger U and Finnis M W 1996 *Phys. Rev.* B **54** 9147–61
[37] Castiglione M J, Wilson M and Madden P A 1999 *J. Phys.: Condens. Matter* **11** 9009–24
[38] Wilson M, Jahn S and Madden P A 2004 *J. Phys.: Condens. Matter* **16** S2795–810
[39] Castiglione M J, Wilson M, Madden P A and Grey C P 2001 *J. Phys.: Condens. Matter* **13** 51–66
[40] Allen M P and Tildesley D J 1986 *Computer Simulations of Liquids* (Oxford: Oxford University Press)
[41] Tuckerman M E and Martyna G J 2000 *J. Phys. Chem.* B **104** 159–78
[42] Rietveld H M 1969 *J. Appl. Crystallogr.* **2** 65–7
[43] Shannon R D 1976 *Acta Crystallogr.* A **32** 751–67
[44] Kato K 1976 *Acta Crystallogr.* B **32** 764–7
[45] Ercit T S 1991 *Mineral. Petrol.* **43** 217–23
[46] Kilo M, Argirusis C, Borchardt G and Jackson R A 2003 *Phys. Chem. Chem. Phys.* **5** 2219–24
[47] Segall M D, Lindan P J B, Probert M J, Pickard C J, Hasnip P J, Clark S J and Payne M C 2002 *J. Phys.: Condens. Matter* **14** 2717–44
[48] Aguado A, Bernasconi L, Jahn S and Madden P A 2003 *Faraday Discuss.* **124** 171–84
[49] Madden P A, Heaton R, Aguado A and Jahn S 2006 *J. Mol. Struct.: Theochem* **771** 9–18
[50] Heaton R J, Madden P A, Clark S J and Jahn S 2006 *J. Chem. Phys.* **125** 144104